Research Article | Vol. 29, No. 21 / 11 Oct 2021 / Optics Express 34394
Optics EXPRESS

Optical bunching of particles in a liquid flow

SALAH AWEL,[1,*] SVEN BOHNE,[2] REZA EBRAHIMIFARD,[3] HOC KHIEM TRIEU,[2] SAŠA BAJT,[3,4] AND HENRY N. CHAPMAN[1,4,5,6]

[1]*Center for Free-Electron Laser Science CFEL, Deutsches Elektronen-Synchrotron DESY, Notkestrasse 85, 22607 Hamburg, Germany*
[2]*Hamburg University of Technology, Eissendorfer Str. 42, 21073 Hamburg, Germany*
[3]*Deutsches Elektronen-Synchrotron DESY, Notkestrasse 85, 22607 Hamburg, Germany*
[4]*The Hamburg Centre for Ultrafast Imaging, Luruper Chaussee 149, 22761 Hamburg, Germany*
[5]*Department of Physics, Universität Hamburg, Luruper Chaussee 149, 22761 Hamburg, Germany*
[6]*Molecular and Condensed Matter Physics, Department of Physics and Astronomy, Uppsala University, Sweden*
[*]*salah.awel@desy.de*

Abstract: High-speed liquid micro-jets are used to rapidly and repeatedly deliver protein microcrystals to focused and pulsed X-ray beams in the method of serial femtosecond crystallography. However, the current continuous flow of crystals is mismatched to the arrival of X-ray pulses, wasting vast amounts of an often rare and precious sample. Here, we introduce a method to address this problem by periodically trapping and releasing crystals in the liquid flow, creating locally concentrated crystal bunches, using an optical trap integrated in the microfluidic supply line. We experimentally demonstrate a 30-fold increase of particle concentration into 10 Hz bunches of 6.4 µm diameter polystyrene particles. Furthermore, using particle trajectory simulations, a comprehensive description of the optical bunching process and parameter space is presented. Adding this compact optofluidics device to existing injection systems would thereby dramatically reduce sample consumption and extend the application of serial crystallography to a greater range of protein crystal systems that cannot be produced in high abundance. Our approach is suitable for other microfluidic systems that require synchronous measurements of flowing objects.

1. Introduction

The method of serial femtosecond crystallography (SFX) uses intense and short (femtosecond-duration) pulses from X-ray free-electron lasers (XFELs), to record many snapshot X-ray diffraction patterns of protein crystals that flow across the focused beam [1,2]. SFX overcomes the problem of radiation damage to the protein structure in conventional protein crystallography by using a short and intense X-ray pulse to record a diffraction pattern before structural modification occurs [3]. This method of out-running radiation damage allows doses that are much greater than can be tolerated in conventional experiments, avoiding the need for large crystals (which are difficult to grow) or cryogenic temperatures (which may modify the structure from the physiologically relevant one). However, the crystal is subsequently vaporized by the X-ray pulse so full diffraction datasets, necessarily recorded at many crystal orientations, must be done by continuously introducing fresh crystals to the X-ray focus. Various methods have been developed to transport crystals that usually range in size from less than 1 µm in diameter to about 20 µm. Some of these transport slurries of crystals across the focus of the X-ray beam using liquid micro-jets [4,5] or micro-columns of crystal-embedded viscous media using extrusion injectors [6], and some continuously scan a solid substrate across the X-ray focus carrying pre-deposited crystals [7,8]. Of these, liquid micro-jets are the most versatile and adaptable, and have been heavily employed in SFX experiments. They enable high throughput experiments with data collected at high rates, including at the megahertz pulse repetition of the European XFEL [9].

#440173 https://doi.org/10.1364/OE.440173
Journal © 2021 Received 13 Aug 2021; revised 29 Sep 2021; accepted 29 Sep 2021; published 6 Oct 2021

Optics EXPRESS

Liquid micro-jets are also very suitable to initiate reaction kinetics, either using the mix-and-inject technique [10] or by direct photo-activation of the crystals [11].

There is often a mismatch between the rate of introduction of crystals in an SFX experiment and the arrival of XFEL pulses. Extrusion injectors and scanned substrates can feed a fresh crystal into the beam at a steady rate of about 0.1 to 10 kHz, to match equally-spaced pulses at facilities such as the Linac Coherent Light Source [12] or SACLA [13], for example, but liquid micro-jets flow at much higher velocities. The European XFEL [14] can generate 27,000 pulses per second, but these are grouped into 10 pulse trains per second with pulses within those trains arriving at rates of 1 to 4 MHz and each train lasting up to 600 µs. Given that the sample must move by about 50 µm between pulses—to clear the debris of the previous pulse—speeds approaching 100 m/s are typically needed. So far, only liquid micro-jets can move the sample at such a speed [15]. However, in the 100 ms between pulse trains, crystals flow that will never be probed by the X-ray beam. A typical duty ratio of the length of the pulse train to the time between trains in an SFX experiment at the European XFEL is 3×10^{-3}. This means that about 300 times the number of crystals must be injected in such an experiment than will contribute to the measured diffraction. There are similar inefficiencies using liquid micro-jets at facilities which produce equally-spaced pulses. Additionally, the crystal slurries used in such experiments require high particle concentration to ensure that when an X-ray pulse does come, there is likely a crystal in the interaction region to receive it. In practice, highly concentrated samples tend to aggregate and clog the capillaries and nozzles used to deliver them. Therefore, most experiments typically run at a lower than optimal concentration, adding further inefficiencies.

The root of these inefficiencies lies in delivering sample into a pulsed X-ray beam with a continuous flow. It is therefore reasonable to seek a pulsed injection method that can deliver crystals synchronized with the arrival of the XFEL pulses. Several attempts have been made in the past to achieve this utilizing piezoelectric [16] and acoustic [17] driven droplet-on-demand injection, segmented flow droplet injection [18] and droplet on tape injection [19]. The inability to maintain stable and continuous synchronization with X-ray pulses and the formation of large droplets or unstable jets are just a few unsolved problems limiting these injection techniques.

Here, we present a novel technique that addresses the inefficiencies of sample delivery by bunching the crystals in a liquid flow, without disturbing the liquid flow itself, using an optofluidics device placed upstream of the nozzle used to create the jet. The basic idea is to optically trap the crystals against the continuously flowing liquid for a short period of time before quickly releasing them into the flow, repeating this process at regular intervals. The released bunches would be equally spaced in time with a phase that is adjusted so that they arrive at the X-ray interaction region coincident with an X-ray pulse. This "catch and release" approach produces locally concentrated crystal bunches, thereby greatly reducing the required initial concentration of crystals and the amount that have to be prepared. The optical trapping is achieved using counter-propagating Gaussian beams, delivered through opposing optical fibers that are perpendicular to the fluid flow in a microfluidic channel. We characterized optical particle trapping through an analysis of measured particle trajectories in the channel, from which the optical forces on the particles were determined. This was used to validate simulations of particle bunching by a trap that modulates in time, by integrating computational fluid dynamics and optical force calculations. We then carried out and analyzed optical particle bunching in our prototype device to validate a numerical exploration of bunching and trapping behaviors as a function of laser power, duty cycle, and liquid flow rate, and found conditions that limit subsequent dispersion of pulses.

2. Optical trapping and bunching

Since first demonstrated by Ashkin [20], optical manipulation of micrometer-sized particles has found application across various fields in life and material sciences, biology, and fundamental

Optics EXPRESS

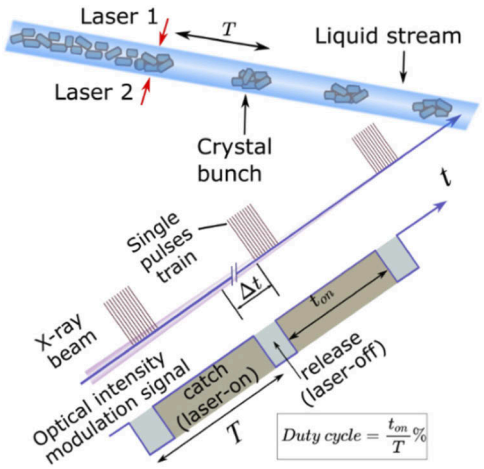

Fig. 1. Timings for particle bunching and synchronization with the XFEL pulses. Pulse structures of the X-ray beam, top, and the optical intensity temporal modulation signal, bottom.

physics. In optical tweezers, a gradient force from a tightly focused Gaussian optical beam is used to trap the particles. However, the working distance of the high numerical-aperture objective required to create the tightly focused beam is too short for our application. In a different configuration, a dual-beam optical trap uses two counter-propagating divergent Gaussian beams to create an intense optical field that traps particles. Besides increasing the working distance, the divergent beam greatly increases the trapping volume and limits the radiation exposure of the trapped particles. This is particularly important when dealing with biological samples. No optics are required other than the fibers, and the dual-beam trap is suitable for integration with a micro-channel located between the opposing fibers to transport the particles. This simple yet effective arrangement offers flexibility to create miniaturized microfluidics and lab-on-chip devices such as in optical stretchers [21], optical binding [22], and optical spanners [23].

In a dual-beam trap, a particle is captured between the two beams by balancing the net scattering and gradient forces of the two lasers, assuming no external forces. At any point in the laser field the force acting on the particle is the superposition of the force contribution from each beam. The scattering forces, or the reaction to the change in momentum of the photons, act in the propagation direction of the beams with a maximum at the fiber tips and a net minimum at the midway point between them (for lasers of equal intensity). Conversely, the gradient forces of both lasers, due to intensity gradients across a particle, add constructively and push particles towards the intensity maximum. To optimize the trapping efficiency, the fiber tips must be close enough to each other to ensure strong forces while still having a large enough gap for the fluid flow, and they must be well aligned to each other, both in position and pointing. The optimum distance between the fibers for a desired trapping volume and channel dimension is dependent on the numerical aperture of the beam, mode field diameter (MFD) of the fiber, and the wavelength of the light [24].

Most dual-beam trapping experiments are performed on particles in liquid suspensions that flow slowly through the device or do not flow at all. The trapping is typically realized with laser powers as small as few tens of milliwatts. However, here, where the particles are captured against a fast-flowing liquid, not only is higher laser power needed, but the setup must also endure the higher energy deposited by the laser beams. In this constant liquid flow, required to ensure a stable and steady micro-jet downstream of the trap, particle bunching is achieved by periodically modulating the optical beams at a frequency matching that of the X-ray pulses or X-ray pulse

Optics EXPRESS

trains as shown in Fig. 1. It is not necessary for the trap to completely arrest the motion of particles, but it should perturb their trajectories to bring them closer together when activated. (Several traps in series could successively reduce the length of bunches.) However, in the "catch and release" scheme, particles are captured during the optical beam on-cycles (i.e., X-ray off) and released back into the flow in the short optical beam off-cycles (i.e., X-ray on). The liquid flow speed determines the delay between particles leaving the trap and arriving at the interaction region. For a given liquid flow the coincident arrival of the crystal bunches with X-ray pulses can be controlled by varying the time delay (Δt) of the optical modulation to the facility master clock (see Fig. 1). Due to Poiseuille flow in the capillary, bunches will disperse after release. To minimize this spread the trap should be close to the nozzle. Pre-focusing the particles to the center of the capillary also minimizes dispersion, as demonstrated below.

3. Experimental

3.1. Optofluidics device fabrication

To fabricate compact optofluidics arrangements, different fabrication techniques have been demonstrated. One approach is to assemble the individual optical and fluidic elements on a glass substrate using either glass, PDMS or two-photon polymerization (2PP) 3D printed structures as an aligning support structure [21–26]. In a completely different approach, a monolithic glass microchip was fabricated using femtosecond laser micromachining technology [27]. We adopted the former approach by assembling individual elements on a 25 mm^2 glass substrate. The fluidics and optical components were positioned using an alignment structure of dimensions of 5 mm × 100 mm × 1 mm (see Fig. 2(a)) fabricated using a 2PP 3D printer (Nanoscribe Photonic Professional GT2, 25× objective). In this structure, a channel of square cross section (205 μm × 205 μm) accommodates a square borosilicate liquid microcapillary (100 μm × 100 μm ID, 50 μm wall thickness, VitroTubes Inc.). Perpendicular to this channel, the 3D-printed structure has two opposite coaxial cylindrical channels (128 μm diameter) with V-grooves to guide and hold the optical fibers centered on the center axis of the square liquid capillary. During assembly, after cleanly cleaving the ends of the optical fibers (125 μm outer diameter), a modest amount of index matching gel was applied on the fiber tips and carefully pushed through the V-grooved channels until they touched the outer walls of the liquid capillary (see Fig. 2 (c)). We typically constructed two optical traps on a single device as shown in Fig. 2(a). In the setup discussed here only one of the two was operated at a time. However, it is possible to operate both traps in synchrony to increase bunching efficiency.

The liquid supply line was connected to a syringe pump (Centoni Low Pressure Syringe Pump, neMESYS 290N) using flexible fused silica capillary tubing (Molex, Polymicro, 100 μm ID and 360 μm OD). Between this supply line and the microfluidics channel a small 2PP 3D-printed adapter union was inserted, with 370 μm ID cylindrical opening on the pump side and 200 μm wide square opening on the optofluidics side. This adapter has two functions: first it interfaces the square fluidic channel to the round supply line. Second, as seen in Fig. 2(b), it also has an inline convergent nozzle (ID = 100 μm inlet and ID = 50 μm aperture and 0.5 mm long) that focuses the particles to the center of the channel before the particles enter the trap. This convergent nozzle is easy to fabricate and has a simple but effective operation. No additional co-flowing fluid is needed to focus the particles. Instead, the focusing mechanism is solely provided by the convergent shape of the nozzle and the liquid flow

The optical beams were supplied by two independent fiber-coupled laser diodes (Thorlabs, BL976-PAG900, 976 nm and 0.9 W each). The lasers were guided by polarization-maintaining optical fibers (SM98-PS-U25A-H, MFD = 6.6 μm), with the polarizations set to be parallel to the direction of fluid flow. Modulation of the optical power was accomplished by modulating the drive current of the diode lasers using a function generator (TG4001, Thurlby Thandar

Optics EXPRESS

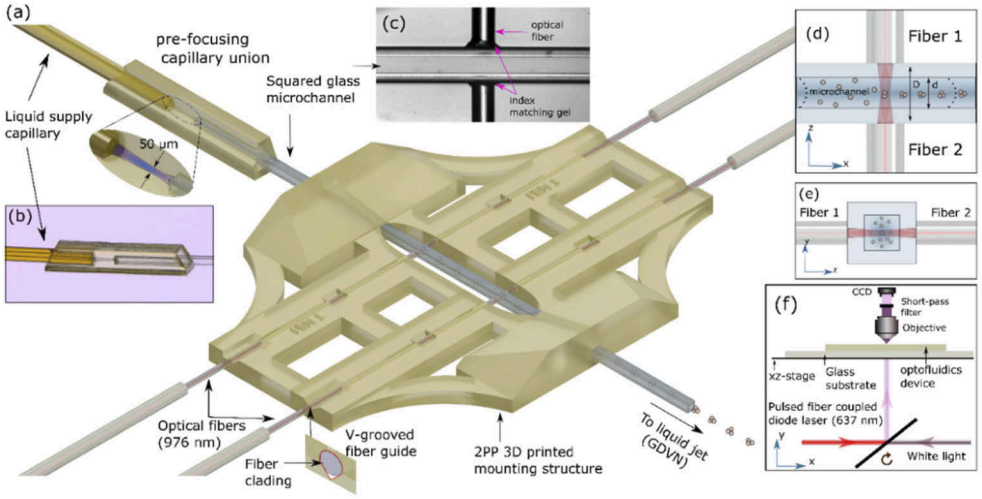

Fig. 2. Optofluidics device assembly. (a) The fluidics and optical components are assembled on a 2PP 3D printed support structure. The device has two independent optical traps separated by 2 mm. However, only one was operated at a time. In the inset to the left the pre-focusing capillary union is shown. (b) Optical microscope image of the pre-focusing nozzle. The interaction region (c) optical microscope image, (d) top view and (e) cross-section view. 'D' and 'd' are the OD (the distance between the fibers) and ID of the channel, respectively. (f) Optical illumination and imaging setup.

Instruments). A single modulation voltage output from the function generator drove both lasers to ensure a perfect temporal synchronization between the two lasers outputs.

3.2. Particle tracking experimental setup

We characterized the performance of the optical buncher by imaging and tracking polystyrene particles in the device as detailed in Sec. 3.4. To track fast-moving particles with the accuracy needed for a dynamics analysis of trajectories, high-resolution images must be recorded with short exposure times and high frame rates. To this end, the entire optofluidics assembly was placed on the sample stage of a commercial microscope that was modified to accommodate two different illumination sources (see Fig. 2 (f)). We utilized either a broadband white light source (Storz Light Source, Xenon Nova 300, for CW illumination) or a fiber-coupled diode laser (DILAS, 10 W, 637 nm, for pulsed illumination). The images were recorded on a CCD camera (Basler Aca2000-165um). The coherent scattered light from the 976 nm trapping beams was prevented from contributing to the images by installing a short-pass filter (Thorlabs, FESH0750, cut-off wavelength 750 nm) in front of the CCD camera.

3.3. Sample preparation

Polystyrene particles were investigated, ranging in size between 2-10 μm. In this paper we focus only on the results obtained using 6.4 μm diameter polystyrene beads. Suspensions of these were diluted to $\approx 7 \times 10^5$ particles/ml in a 12.5% pure sucrose solution to achieve neutral buoyancy to prevent particles from settling during extended measurements. The properties of the sucrose medium were: density 1.05 g/ml [28], dynamic viscosity 1.45×10^{-3} Pa·s [29], and refractive index 1.352 [28]. These optical and fluidic properties of the medium are fairly close to pure water. Therefore, trapping polystyrene particles in this medium does not significantly alter the trapping efficiency.

Optics EXPRESS

3.4. Particle tracking analysis

Experimental particle trajectories were extracted from microscope images taken at uniform frame rates. From the trajectory of a particle, its velocity and acceleration could be obtained, from which the optical force, liquid velocity field, and hence the drag force is found (see Sec. 5.1). A particular trajectory was mapped by tracking the same particle from frame to frame by the following steps: First, the noise in every image was reduced by applying a bandpass filter with a kernel size comparable with the particle size. This was followed by subtracting a static background obtained using the first 100 frames. Next, an experimentally determined intensity threshold was applied to the background-subtracted grey value image and segmented into connected pixels representing a single particle. Then the coordinate of the center of each particle in every frame was located by calculating the intensity centroid of the connected pixels. These positions were stored together with the frame number. Using this method, we were able to localize the particle position with uncertainty <1 μm. In the final step, the particle positions were linked over successive frames using an open source python module [30]. A detailed exposition of particle locating and linking techniques can be found elsewhere [31].

4. Numerical Lagrangian particle tracing in a fluid and an optical field

We present a model used to simulate the dynamics of particles subjected to forces of the liquid flow and optical fields in the microfluidics channel. Throughout this paper we use a right-handed coordinate system with an origin at the intersection of the channel and the common central axis of the optical beams. The optical forces point toward the origin from all directions and thus, in the absence of the liquid flow, an optically trapped particle will be located at the origin. We define the direction of flow as the x axis and take the laser beams to be parallel to the z axis, so that the plane of the device is x-z and the cross section of the fluid channel is the y-z plane. Liquid flow in the channel is fastest on axis and follows the square symmetry of the channel cross section. Together with the radial optical forces, particles on a central orthogonal plane of the channel (spanning y=0 or z=0) will always remain in that plane after being acted upon. Hence, it is sufficient to treat the motion as separable in y and z coordinates and simulate the motion of particles in either of these 2D planes. Since the polarizations of the lasers are aligned to the x axis we performed the simulation in x-z plane, which is also what is imaged in the microscope. We assume that only one particle was present in the optical field at a given time, ignoring interactions between particles and optical binding. Our experiments matched this condition by using a low concentration of particles.

To model the two-phase flow problem, i.e. the particle and the carrier liquid flow, we used the Lagrangian-Eulerian description of the particle motion. In this approach, the discrete particle motion is found by solving a set of ordinary differential equations given by the Newtonian equation of motion, while solving the continuous background liquid properties along the trajectory [32]. The motion of a micro-particle moving through the fluid with velocity field $v_f(z)$ and optical field $F(x,z)_{\mathrm{Opt}}$ can be described by the following Newtonian equations of motions:

$$m_p \frac{dv_p(x,z)}{dt} = F(x,z)_{\mathrm{Drag}} + F(x,z)_{\mathrm{opt}} + F_{\mathrm{others}} \tag{1}$$

$$v_p(x,z) = \frac{dr(x,z)}{dt} \tag{2}$$

$$F(x,z)_{\mathrm{drag}} = \frac{m_p}{\tau_p}(v_f(z) - v_p(x,z)) \tag{3}$$

where m_p and v_p are mass and velocity of the particle, respectively and τ_p is the particle velocity response time which determines the time it takes for a particle to reach the local fluid velocity. F_{others} represents other forces, such as those due to gravity and buoyancy, which are not

Optics EXPRESS

considered in our calculations. For a spherical particle of diameter d_p in a low Reynolds number flow, the drag force, F_{drag}, can be expressed as the Stokes drag equation using the response time given by

$$\tau_p = \frac{\rho_p d_p^2}{18\eta} \tag{4}$$

where, η is the dynamic viscosity of the fluid and ρ_p is the density of the particle.

The liquid flow in the fluidic channel is characterized by a very small Reynolds number and we consider situations with particle concentrations well below 1%. This means that, given the small size of the particles we are investigating, the effect of the particles on the fluid flow can be ignored (one-way coupling) [33]. This assumption simplifies the simulation by decoupling the fluid and particle motions. Furthermore, we assume that the short and localized exposure to the optical field does not affect the bulk fluid properties. Hence, the liquid flow field and the optical field can also be treated separately. This significantly reduces the computational time by permitting us to pre-calculate the velocity and optical fields before Eq. (1) and Eq. (2) are solved.

4.1. Fluid velocity field calculations

The liquid flow field in the channel can be determined experimentally or for simple channel geometry like ours, it can also be calculated numerical by solving the Navier–Stokes equations using finite-element solver, such as COMSOL Multiphysics [34]. In these simulations we employed an experimental approach known as particle image velocimetry (PIV) [35], where the fluid velocity is computed by tracking the motion of multiple micro-particles flowing through the liquid stream in the y=0 plane of the channel (with laser beams turned off and particles imaged with a small depth of focus). Figure 3(c) shows the velocity profile of a sucrose solution with a flow rate of 0.5 µl/min, giving a speed of 1.5 mm/s in the middle of the channel. The profile has the typical parabolic velocity distribution of Poiseuille flow with zero velocity at the capillary walls and maximum velocity in the center of the channel. In our simulations we represented the liquid velocity with a fitted parabolic function.

4.2. Optical force field calculations

When the diameter of a particle is similar to or larger than the optical wavelength, its interaction with the laser field can be modelled using either geometrical optics or the generalized Lorenz–Mie (GLM) theory. We used the GLM method, since we found it gave more accurate results, and adopted an open source Matlab computational toolbox for optical tweezers [36]. We modified the software code to simulate particles trapped by two counter-propagating diverging Gaussian beams, each with a beam waist of $\omega_0 = 3.3$ µm ($\omega_0 = \text{MFD}/2$), passing through three different media of index matching gel, borosilicate glass and the flowing medium, i.e. sucrose (see Fig. 2(c-e)). We used the refractive index at a wavelength of 976 nm of n_{sucrose}=1.352 [28], n_{BSG}=1.462 [37], and n_{gel}=1.4462 for sucrose, borosilicate glass and index matching gel, respectively.

For simulating particle trajectories, optical forces are first calculated on points in the channel on a grid in the x-z plane to produce a force field. One such example is depicted in Fig. 3(a), where the combined force on 6.4 µm diameter polystyrene particles from both beams is plotted for the case when the output of each fiber is 400 mW. Calculations of particle trajectories then use interpolated forces from this grid. In principle, optical forces could also be calculated directly at each position of the particle as its trajectory is calculated in time. However, this significantly increases the computation time.

4.3. Particle trajectories

To fully trace the trajectory $r(t)$ of a particle, Eq. (1) and Eq. (2) must be solved twice at each simulation time point, i.e., once for each vector component of the particle motion. The particle

Optics EXPRESS

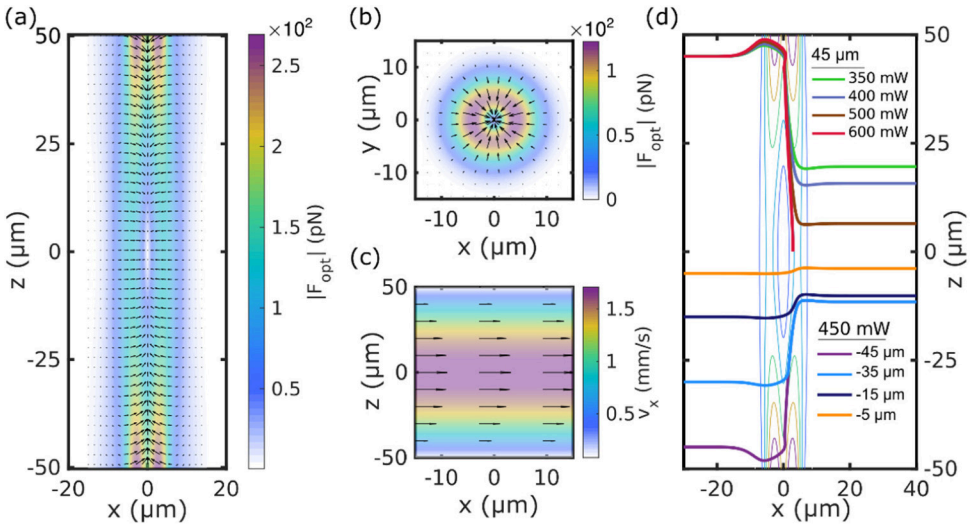

Fig. 3. Calculated force fields and particle trajectories. The optical force exerted by the counter propagating 400 mW Gaussian beams on 6.4 μm polystyrene particle (a) the cross-section at y=0 and (b) the cross-section at z = 0. The colorbar and the arrows represent the magnitude and direction of the optical forces, respectively. (c) Axial fluid velocity profile produced by a sucrose solution flowing at 0.5μl/min. (d) Simulated 6.4 μm polystyrene particle trajectories. The top half of the figure shows the trajectories of the particle, which was started at a fixed position of z=+45 μm and was subjected to different optical powers. In the bottom half of the figure particles started at different radial offsets and were exposed to a fixed power of 450 mW from each fiber. The extent of the optical field in the channel is indicated by the contour plot of the force field magnitude.

position $r(t_i + \Delta t)$ at a given time point $t_i + \Delta t$ is determined using two coupled steps; first the analytical solution of Eq. (1) is used to give the velocity of the particle at time $t_i + \Delta t$, using the information calculated at the prior time step t_i, i.e., the particle current position $r(t_i)$, velocity $v(t_i)$, optical force $F(r(t_i))_{\text{opt}}$ and liquid velocity $v_f(r(t_i))$. In the second step, the position of the particle $r(t_i + \Delta t)$ is found solving Eq. (2) using the midpoint method, as

$$r(t_i + \Delta t) = r(t_i) + \frac{(v_p(t_i + \Delta t) + v_p(t_i))}{2}\Delta t. \tag{5}$$

The process repeats over time steps t_i until the particle trajectory is fully traced or a specified time is reached.

Figure 3(d) shows simulated trajectories of 6.4 μm diameter polystyrene particles suspended in a sucrose solution flowing at 0.5 μl/min. The contour plot shows the magnitude of the optical force (from Fig. 3(a)) and the solid lines are the trajectories of the particles. In the top half ($z > 0$) the trajectories are plotted for a particle introduced at a fixed position of $z = 45$ μm and exposed to different optical powers. In the laser field, the particles are pushed by the scattering force of the laser toward the center of the channel where the drag force of the liquid is stronger than the gradient force of the laser. As shown in Fig. 3(a) and (b) optical forces act toward the origin of the coordinate from every direction whereas the drag force acts only in the flow direction (Fig. 3(c)). Therefore, using sufficiently high laser power it is possible to trap a particle by balancing the gradient force of the lasers and the drag force. This is shown by the red curve in Fig. 3(d) which assumed 600 mW power in each fiber. It is interesting to note that the equilibrium position of the trapped particle is not in the center of the beams but rather at an offset determined by the laser intensity and the magnitude of the drag force. In the bottom half of Fig. 3(d) ($z < 0$) the

Optics EXPRESS

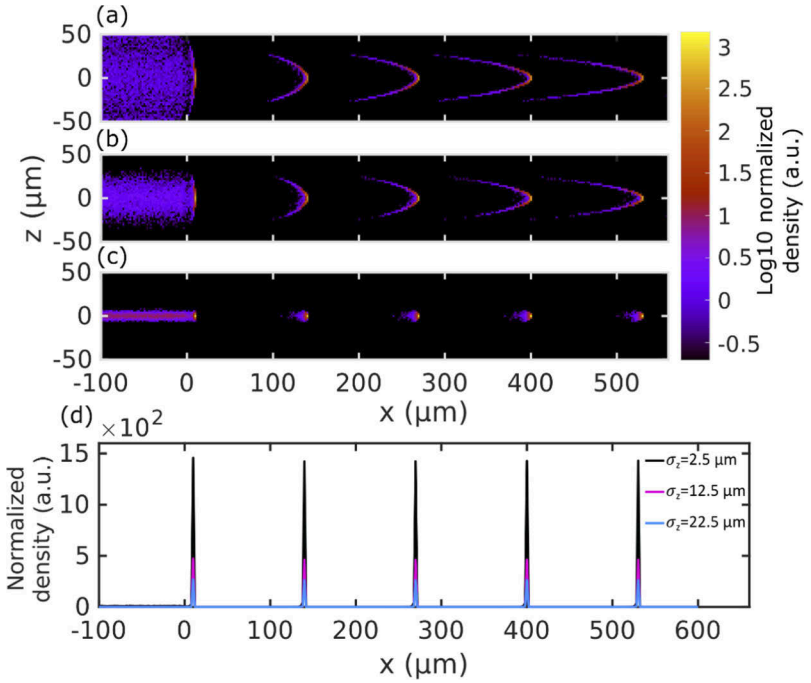

Fig. 4. Particle bunching simulations using 6.4 μm particle beams introduced with different lateral distributions. 2D particle densities when the particles were emitted with a normal density distributions center at z=0 and standard deviation of (a) 22.5 μm, (b) 12.5 μm and (c) 2.5 μm. (d) Linear plot of the particle densities in (a)-(c) along the channel axis. The lasers are located at $x = 0$ and propagate in the z-direction.

trajectories are shown of particles introduced at various positions in the channel of z = -5 μm, -15 μm, -30 μm, -45 μm, all at a fixed 450 mW optical power per fiber.

4.4. Particle bunching simulations

Particle bunching requires the optical power to be turned on and off periodically. This can be simulated by introducing a modulation function, $\Pi(t)$, in Eq. (1). Typically, the modulation signal has a rectangular waveform and it is characterized by the pulse duty cycle (DC) and the modulation period (T) (see Fig. 1). For a single period of the modulation signal the modulated optical field is given by:

$$F(x, 0, z, t)_{\text{opt}} = F(x, 0, z)_{\text{opt}} \cdot \Pi(t) \tag{6}$$

$$\Pi(t) = \begin{cases} 1, & t \le T \cdot DC \\ 0, & T \cdot DC < t < T \end{cases} . \tag{7}$$

Using the modulated optical force given in Eq. (6), the trajectories of periodically caught and released particles were found using similar steps described above. To reveal the particle bunching effects, the trajectories of multiple particles with initial positions randomly distributed in the channel upstream of the trap were computed. The particle bunch information was obtained by summing contributions from different particles.

Figure 4 shows the result of the 10 Hz particle bunching simulation of 6.4μm diameter polystyrenes introduced with different lateral distributions into the modulated trap. In these simulations, we assumed that the particles had neutral buoyancy in a sucrose solution flowing at

Optics EXPRESS

400 nl/min and that a 460 mW optical power with 97.5% duty cycle at 10 Hz was applied per fiber. In each of the simulations, 10^4 particles were emitted at random times at $x = -100$ μm with transverse coordinates sampled from normal distributions centered at $z = 0$ and with half-widths σ_z = 22.5, 12.5 and 2.5 μm. The calculated trajectories were synchronously sampled with the rising edge of the 10 Hz modulation signal. Then the resulting particle positions were accumulated into 2 μm × 2 μm bins and normalized to the mean axial particle density measured upstream of the trap in Fig. 4(a) to produce the 2D particle density maps shown in Fig. 4(a), (b) and (c). These simulations predict that a wider initial particle beam produces wider bunches which then disperse in the flow with a parabolic profile of the liquid flow filed (see Fig. 4 (c)). In the simulations, a particle beam pre-focused to 2.5 μm half-width gave a four-fold increase in particle density compared with an unfocused beam as seen in Fig. 4(d). These particle trajectory and bunching simulations agree well with the experimental observations, as we will show in the next section.

Using this particle bunching simulation approach we can now predict the behavior of particle bunching for a particular laser field distribution, laser power, particle size, buoyancy, channel geometry, flow rate, bunching frequency and duty cycle. In Fig. 5 we show the results of simulations carried out for various values of two of these parameters—laser power and flow rate—for 6.4 μm diameter polystyrene particles, bunching at 10 Hz with 95% duty cycle using the same trap geometry as above. The plot shows the peak particle density in a bunch downstream of the trap, 20 ms after release. For each pair of values of laser power and flow rate, the trajectories of 10^3 particles were simulated to obtain an estimate of the particle density.

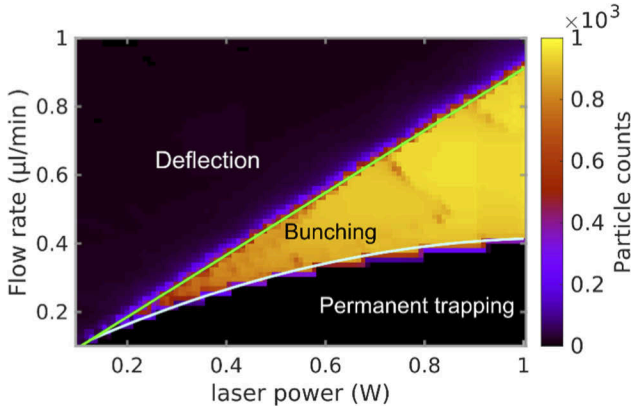

Fig. 5. Simulated laser power-flow rate parameter space diagram of 6.4 μm diameter polystyrene particle bunching. In these simulations the laser intensity was modulated by 10 Hz and 95% duty cycle modulated signal. The green line marks the boundary between particle deflection and trapping, and the white between particle bunching and permanent trapping.

Three distinct regions in the parameter space of Fig. 5 can be seen. At flow rates that are too high for a particular laser power, particles are deflected but are not appreciably slowed down in the trapping region. In this region, labelled "Deflection" in Fig. 5, modulating the power at 10 Hz causes a modulation of the density of the particle stream, but with very low contrast. When laser powers are too high for a particular flow rate, particles are recaptured by the trap when it turns on again for the next bunch. In this region, labelled "Permanent trapping", no particles are emitted downstream (although in practice particles may eventually escape when many accumulate in the trap). Efficient bunching occurs between these two cases in the region labelled "Bunching", which is delineated by the green line at too high flow rate or too low laser power and the white line at too low flow rate or too high laser power. In this region the bunch particle density is roughly

Optics EXPRESS

constant. We find that the transition between bunching and deflection depends on a simple ratio of flow rate to laser power. The proportionality depends on the relative strengths of the optical and drag forces on the particles and hence will depend on particle properties such as size and refractive index. The transition between bunching and permanent trapping approximately follows the ratio of flow rate squared to laser power. That is, if the flow rate is doubled, the tolerable laser power to achieve bunching can be increased four times. This transition depends on the duty cycle of the trap modulation, which can be adjusted to accommodate a particular flow rate. However, given that it is preferable to work at the lowest possible laser power, it is recommended to operate near the boundary between deflection and bunching.

5. Experimental measurements

5.1. Optical force measurements using particle trajectories

To measure the optical forces on particles, using the set-up described in Sec. 3.2 we operated the lasers at a constant (unmodulated) laser power of 65 mW from each fiber in combination with a low sample flow of 50 nl/min. This power was lower than used in the subsequent bunching measurements to avoid heating the medium and changing temperature-dependent parameters such as viscosity. We carried out measurements at room temperature. The liquid flow rate was set to create a drag force just high enough so that particles were not permanently trapped by the laser. The microscope objective was focused in a plane at the center of the channel so that only particles in that plane were tracked and used for characterization. This enables us to compare the 2D simulated and measured trajectories. The measured trajectory of a 6.4 μm diameter polystyrene particle is shown in Fig. 6. A composite stroboscopic image of the particle recorded with a 40x objective is shown in Fig. 6(a). This image is the superposition of 66 sequential frames recorded every 20 ms, each with an exposure time of 500 μs. The white crosses represent the particle centroids (see Sec. 3.4) which are also plotted in Fig. 6(b) as the pink open circles. The velocity components as a function of time, obtained from these measured positions, are shown by the open circles in Fig. 6(c). By comparing the x component to the fluid velocity field v_f (appropriately scaled from that shown in Fig. 3), we obtained the experimentally-determined drag force. Then, taking the derivative of the particle velocities to yield acceleration components, the components of the optical forces on the particle were found using Eq. (1) and the estimated particle mass [38]. These optical force components are shown as open circles in Fig. 6(d). Prior to entering the optical field ($x < -0.02$ mm), the particle does not have any lateral motion (similar to the fluid velocity shown in Fig. 6 (c)). Upon entry to the field, the particle is deflected up by the scattering force ($F(x,z)_{\mathrm{opt-z}}$) of the lower laser to a position in the channel where the local drag force is greater than the counter gradient force ($F(x,z)_{\mathrm{opt-x}}$) produced by the superposition of the two lasers. The particle then leaves the trap at a new lateral position with a final velocity of 0.17 mm/s, which is given by the fluid velocity at that new lateral position (and which is higher than its initial velocity).

We compared the measured trajectory to a prediction using the theoretically calculated optical force field shown in Fig. 3(a) and the measured velocity field of Fig. 3(c). The optical forces were scaled from 400 mW in that figure to 65 mW and reflection loss at the fiber, capillary wall and liquid interfaces were accounted for. The trajectory was obtained by integrating Eq. (1) using the initial measured particle position ($z(t_0)$ = -0.033 mm) and velocity ($v_x(t_0) = 0.1$ mm/s). This predicted trajectory, plotted as a solid line in Fig. 6(b), agrees well with the measurements (open circles). Similarly, a high degree of temporal agreement between the predicted and measured positions is also found (see Supplement 1 Fig. S4). The predicted velocities and forces are shown in Fig. 6(c) and (d) by the blue and orange solid lines. Figure 6 (d) shows a slight deviation between the measured and predicted forces, particularly in the region $-0.02 < x < 0$. One possible explanation for this is a reduced sharpness of the images of particles in Fig. 6(a) as they enter the laser field. This might indicate a component of motion in the y direction which would

Optics EXPRESS

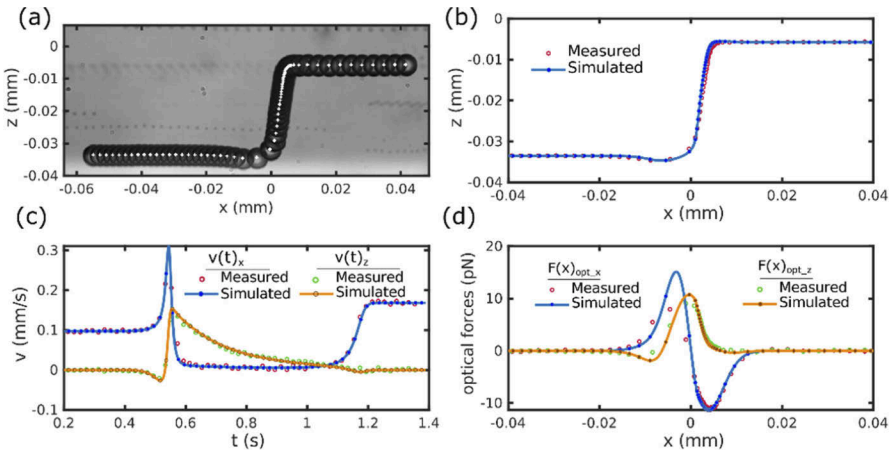

Fig. 6. Analysis of a measured and simulated 6.4 μm diameter polystyrene particle trajectory. The sample was suspended in sucrose solution, which was flowing at 50 nl/min. 65 mW power was applied in each fiber. (a) Stroboscopic image of the particle. The white crosses on the particles represent the particle centroids. Comparison of measured and simulated particle positions (b), velocities (c) and the resulting optical forces (d). The measured points and simulated curves are represented by empty circles and solid lines, respectively.

underestimate the forces acting on the particle. Another source of error could be the uncertainty in the particle centroid determination and its impact on estimates of acceleration.

5.2. *Optical bunching of particles*

The agreement between measured and simulated trajectories implies that the bunching behaviour seen in the simulaltions should be achievable. We recorded short-exposure images at a frame rate synchronized with the bunching frequency of 5 Hz and 10 Hz, with 6.4 μm diameter polystyrene particles. For the 5 Hz series the laser power in each fiber was 260mW with a 95% duty cycle, to operate in the bunching regime. In each cycle the optical trap was active for 190ms. The 10 Hz series used twice the flow (0.4 μl/min) and almost twice the laser power, which was adjusted to 460 mW per fiber at a 97.5% duty cycle. The 10 Hz measurement used similar parameters to those of the simulated 10 Hz bunching series of Fig. 4(a)-(c). A low particle concentration was used, such that at most one particle was trapped in a single modulation period. Particle positions were extracted from >15000 microscope frames, each with a 500 μs exposure time. We recorded images for each series at the phase of the bunching cycle just prior to the deactivation of the trap.

A superposition of a small number of raw frames from the 5 Hz bunching series is shown in Fig. 7(a), with the position of the laser trap indicated at $x = 0$. Time-integrated 2D particle density maps were produced using all frames, and are shown in Fig. 7(b) for 5 Hz bunching and in Fig. 7(e) for the 10 Hz bunching. These histograms were generated by partitioning the measured centroid positions into 3 μm × 3 μm bins. The resulting maps were normalized to the mean axial particle density upstream of the trap to account for differences in the number of frames, sample concentration, and flow rate used in the two series. It is seen that in these upstream regions ($x < 0$) particles were uniformly distributed along the length of the channel but were confined within a width of about 40 μm about the channel center. Downstream of the trap, well-defined particle bunches can be seen with a spacing equal to the product of the bunching frequency and the velocity of the fluid. Linear plots of the gain in particle density along the channel axis are shown in Fig. 7 (c) and (f). A small fraction of the particles is seen to be located outside the bunches in Fig. 7(b) and (e). Some of these may be particles at heights y that passed

Optics EXPRESS

below or above the trapping volume and yet still contributed to the centroid analysis. The plots of Figs. 7(c) and (f) show how many particles travel along the center-line but do not show the total particle flux passing through the channel at a given time and position, which is found by integrating the plots of Figs. 7(b) and (d) along the z direction.

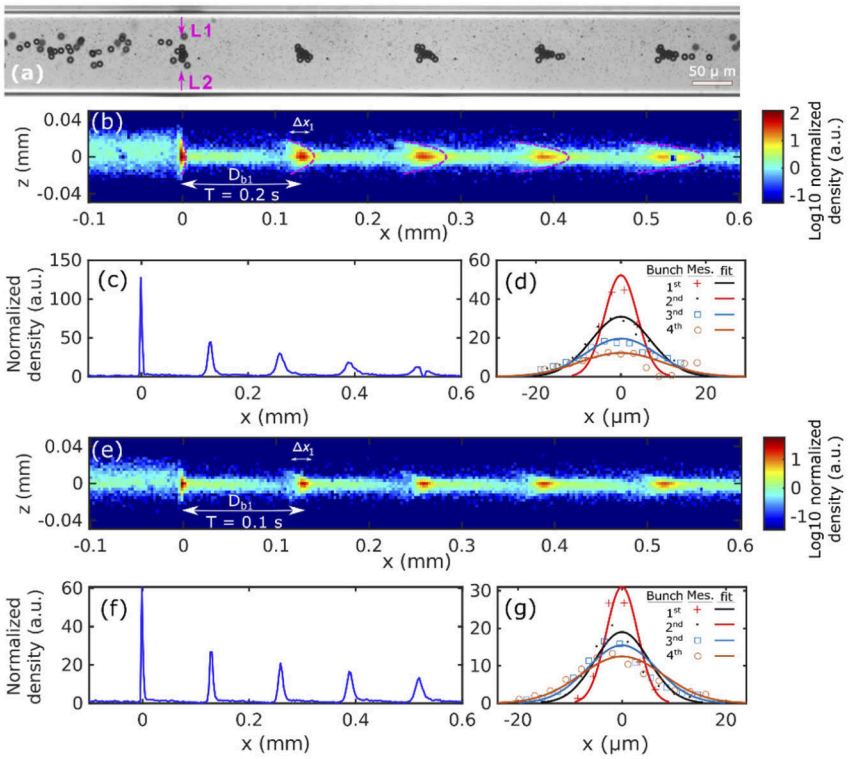

Fig. 7. 5 Hz and 10 Hz bunching of 6.4 μm diameter polystyrene particles. (a) Superposition of selected raw particle images recorded synchronized with the 5 Hz modulated signal, the lasers positions are indicated by the two arrows. (b) 2D normalized particle density generated by accumulating particle positions bunched at 5 Hz. 260 mW power was used in each fiber and sample was flowing at 0.2 μl /min. (c) The axial cross-section of the particle density in (b) at $z = 0$. (d) Axial density distribution of the bunches in (c) are plotted together. (e) Normalized 2D particle density for particles bunched using 10 Hz modulated 460 mW optical powers. Here, the sample was flowing at 0.4 μl /min. (f) The axial cross-section of the particle density in (e) at $z = 0$. (g) Axial density distribution of the bunches in (f) are plotted together. In (d) and (g) the markers show the measured points and the normal distribution fitted densities are represented by the solid lines.

As shown in Fig. 7(c), the 5 Hz bunching increased particle density in the trapping region by more than two orders of magnitude. However, some particles are re-captured in the trap, causing them to be counted more than once to overestimate the particle density near $x = 0$. The particle density in the bunch can be tracked as it propagates from the trap and it is seen that 200 ms after the release the density is 50 times higher than for the incoming particles. This is actually higher than the 20 times expected from the 95% duty cycle because the trap also compresses the particle beam laterally. Similarly, with 10 Hz bunching, the particle density in the bunch at 100 ms after release is about 30 times the particle density before the trap (see the linear density plot in Fig. 7(f)). One may expect that the higher duty cycle of 97.5% used for the 10 Hz bunching

Optics EXPRESS

would double the bunch density, but this is offset by the higher frequency (particles are split into twice the number of bunches) and the higher flow rate.

Once the particle bunch is released from the trap it moves along the channel with the velocity of the liquid. Due to the profile of the fluid flow across the width of the channel (see Fig. 3(c)) the particles on axis pull ahead of those off the axis, resulting in a parabolic leading edge of the bunch shown in Fig. 7(b). Clearly the wider the bunch the greater the dispersion, and thus the pushing of particles to the channel center by the action of the trap helps to reduce dispersion. As noted above, the width can be controlled independently of the bunching by pre-focusing the particle beam. The experimental results of Fig. 7 were actually obtained using the in-line-convergent nozzle (see Fig. 2(a) and (b)). The effect of the focusing nozzle can be seen in the upstream ($x < 0$) lateral distributions of the particles in Fig. 7(b) and (e), where the half-widths of the initial particle beams were 35 μm and 25 μm, respectively. As it is demonstrated in Fig. 4(d), highest particle density in the bunches requires tighter incident particle beam. To achieve this using the in-line-focusing nozzle one must increase the liquid flow rate or reduce the aperture of the nozzle. However, smaller nozzles increase the risk of clogging making other possible methods, such as acoustic focusing [39] or hydrodynamic focusing [40], attractive options. Beside this, pre-focusing is essential for bunching at high repetition rates when the trapping time is not long enough to push particles to the channel center.

6. Conclusions and outlook

Numerical and experimental results were presented of the bunching of flowing particles in a microfluidic channel, using a strategy of "catch and release" with a modulating optical trap. By computing the trajectories of particles influenced by fluidic and optical forces we simulated the particle bunching process and determined how parameters such as flow rate, laser power, and modulation duty cycle govern the bunching. A plot of the bunching efficiency versus laser power and flow rate showed discrete phases of permanent trapping (at low flow and high power), bunching, and deflecting without bunching (at high flow and low laser power). These results served as the basis for the construction of an optimized optofluidics device, used to experimentally demonstrate particle bunching in excellent agreement with simulations.

The results presented here show the potential to increase the efficiency and reliability of sample delivery in serial crystallography experiments. We plan further studies to introduce and optimize optical bunching for crystallography measurements, and expect that the forces exerted on protein crystals are similar to those exerted on polystyrene particles of similar size. The bunching frequency of 10 Hz demonstrated here matches the bunch frequency of the European XFEL [14], and durations of the particle bunches are well matched to the longest duration of 600 μs of the pulse trains at that facility. The increase in particle density obtained by bunching particles should transfer directly to an expected increase in the rate of diffraction patterns acquired in an SFX experiment. To reduce the effects of the dispersion of bunches, the optical buncher should be placed as close as possible to the nozzle. Current nozzle designs [15] allow placing such a device about 0.5 mm from the nozzle exit. Thus, the required particle density of the delivered sample could be dramatically reduced from that used in current SFX experiments (by about 20 times) without loss of measurement rate, which would translate into a 20-times reduction in protein consumed in such a measurement. The lower particle density would also reduce interruptions due to clogging of sample in the sample-feed capillary.

The sample flow rate demonstrated here was 0.4 μl/min when using 460 mW laser power in each fiber. Higher liquid speed requires higher laser power to trap particles against the flow, but higher powers may be damaging to protein crystals (calculations of the accumulated exposures to particles are given in the Supplement 1). Alternatively, bunching with higher liquid flows could be achieved in several ways. Placing several traps in series could successively increase bunch density, without the need to stop the particles against the flow, similar to bunching of electrons in

Optics EXPRESS

a free-electron laser [41]. This requires synchronizing the traps to the particular flow speed, as well as to the X-ray pulses. Another approach is to increase the channel cross-sectional area in the vicinity of the trap to reduce the speed of the liquid.

Beside controlling the flow crystals, this optofluidics device could also be used to monitor crystal concentration during the SFX measurements, by measuring particle scattering picked up by the optical fibers. In addition to already mentioned SFX application, these experimental and theoretical results are of great interest for applications where controlled sample delivery is required, such as in controlled drug delivery, cell manipulation and controlled microfluidic mixing. Furthermore, the particle property dependent trapping strength of the optical buncher can also be exploited to sort different particle species suspended in a flow.

Funding. DESY strategy funds (DSF); Deutsche Forschungsgemeinschaft; the HGF through the Helmholtz International Laboratory on Reliability, Repetition, and Results at Advanced X-ray Sources (HIR3X, InternLabs-0011); Hamburg Centre for Ultrafast Imaging (EXC 2056 - project ID 390715994).

Acknowledgment. We thank DESY (Hamburg, Germany), a member of the Helmholtz Association HGF, for support.

Disclosures. The authors declare no conflicts of interest.

Data availability. Data underlying the results presented in this paper are not publicly available at this time but may be obtained from the authors upon reasonable request.

Supplemental document. See Supplement 1 for supporting content.

References

1. S. Boutet, L. Lomb, G. J. Williams, T. R. M. Barends, A. Aquila, R. B. Doak, U. Weierstall, D. P. DePonte, J. Steinbrener, R. L. Shoeman, M. Messerschmidt, A. Barty, T. A. White, S. Kassemeyer, R. A. Kirian, M. M. Seibert, P. A. Montanez, C. Kenney, R. Herbst, P. Hart, J. Pines, G. Haller, S. M. Gruner, H. T. Philipp, M. W. Tate, M. Hromalik, L. J. Koerner, N. van Bakel, J. Morse, W. Ghonsalves, D. Arnlund, M. J. Bogan, C. Caleman, R. Fromme, C. Y. Hampton, M. S. Hunter, L. C. Johansson, G. Katona, C. Kupitz, M. Liang, A. V Martin, K. Nass, L. Redecke, F. Stellato, N. Timneanu, D. Wang, N. A. Zatsepin, D. Schafer, J. Defever, R. Neutze, P. Fromme, J. C. H. Spence, H. N. Chapman, and I. Schlichting, "High-Resolution Protein Structure Determination by Serial Femtosecond Crystallography," Science **337**(6092), 362–364 (2012).
2. H. N. Chapman, P. Fromme, A. Barty, T. A. White, R. A. Kirian, A. Aquila, M. S. Hunter, J. Schulz, D. P. DePonte, U. Weierstall, R. B. Doak, F. R. N. C. Maia, A. V Martin, I. Schlichting, L. Lomb, N. Coppola, R. L. Shoeman, S. W. Epp, R. Hartmann, D. Rolles, A. Rudenko, L. Foucar, N. Kimmel, G. Weidenspointner, P. Holl, M. Liang, M. Barthelmess, C. Caleman, S. Boutet, M. J. Bogan, J. Krzywinski, C. Bostedt, S. Bajt, L. Gumprecht, B. Rudek, B. Erk, C. Schmidt, A. Hömke, C. Reich, D. Pietschner, L. Strüder, G. Hauser, H. Gorke, J. Ullrich, S. Herrmann, G. Schaller, F. Schopper, H. Soltau, K.-U. Kühnel, M. Messerschmidt, J. D. Bozek, S. P. Hau-Riege, M. Frank, C. Y. Hampton, R. G. Sierra, D. Starodub, G. J. Williams, J. Hajdu, N. Timneanu, M. M. Seibert, J. Andreasson, A. Rocker, O. Jönsson, M. Svenda, S. Stern, K. Nass, R. Andritschke, C.-D. Schröter, F. Krasniqi, M. Bott, K. E. Schmidt, X. Wang, I. Grotjohann, J. M. Holton, T. R. M. Barends, R. Neutze, S. Marchesini, R. Fromme, S. Schorb, D. Rupp, M. Adolph, T. Gorkhover, I. Andersson, H. Hirsemann, G. Potdevin, H. Graafsma, B. Nilsson, and J. C. H. Spence, "Femtosecond X-ray protein nanocrystallography," Nature **470**(7332), 73–77 (2011).
3. R. Neutze, R. Wouts, D. van der Spoel, E. Weckert, and J. Hajdu, "Potential for biomolecular imaging with femtosecond X-ray pulses," Nature **406**(6797), 752–757 (2000).
4. D. P. DePonte, U. Weierstall, K. Schmidt, J. Warner, D. Starodub, J. C. H. Spence, and R. B. Doak, "Gas dynamic virtual nozzle for generation of microscopic droplet streams," J. Phys. D: Appl. Phys. **41**(19), 195505 (2008).
5. D. Oberthuer, J. Knoška, M. O. Wiedorn, K. R. Beyerlein, D. A. Bushnell, E. G. Kovaleva, M. Heymann, L. Gumprecht, R. A. Kirian, A. Barty, V. Mariani, A. Tolstikova, L. Adriano, S. Awel, M. Barthelmess, K. Dörner, P. L. Xavier, O. Yefanov, D. R. James, G. Nelson, D. Wang, G. Calvey, Y. Chen, A. Schmidt, M. Szczepek, S. Frielingsdorf, O. Lenz, E. Snell, P. J. Robinson, B. Šarler, G. Belšak, M. Maček, F. Wilde, A. Aquila, S. Boutet, M. Liang, M. S. Hunter, P. Scheerer, J. D. Lipscomb, U. Weierstall, R. D. Kornberg, J. C. H. Spence, L. Pollack, H. N. Chapman, and S. Bajt, "Double-flow focused liquid injector for efficient serial femtosecond crystallography," Sci. Rep. **7**(1), 44628 (2017).
6. U. Weierstall, D. James, C. Wang, T. A. White, D. Wang, W. Liu, J. C. H. Spence, R. Bruce Doak, G. Nelson, P. Fromme, R. Fromme, I. Grotjohann, C. Kupitz, N. A. Zatsepin, H. Liu, S. Basu, D. Wacker, G. Won Han, V. Katritch, S. Boutet, M. Messerschmidt, G. J. Williams, J. E. Koglin, M. Marvin Seibert, M. Klinker, C. Gati, R. L. Shoeman, A. Barty, H. N. Chapman, R. A. Kirian, K. R. Beyerlein, R. C. Stevens, D. Li, S. T. A. Shah, N. Howe, M. Caffrey, and V. Cherezov, "Lipidic cubic phase injector facilitates membrane protein serial femtosecond crystallography," Nat. Commun. **5**(1), 3309 (2014).

Optics EXPRESS

7. A. Zarrine-Afsar, T. R. M. Barends, C. Müller, M. R. Fuchs, L. Lomb, I. Schlichting, and R. J. D. Miller, "Crystallography on a chip," Acta Crystallogr D Biol Crystallogr **68**(3), 321–323 (2012).
8. M. S. Hunter, B. Segelke, M. Messerschmidt, G. J. Williams, N. A. Zatsepin, A. Barty, W. Henry Benner, D. B. Carlson, M. Coleman, A. Graf, S. P. Hau-Riege, T. Pardini, M. Marvin Seibert, J. Evans, S. Boutet, and M. Frank, "Fixed-target protein serial microcrystallography with an X-ray free electron laser," Sci. Rep. **4**(1), 6026 (2015).
9. M. O. Wiedorn, D. Oberthür, R. Bean, R. Schubert, N. Werner, B. Abbey, M. Aepfelbacher, L. Adriano, A. Allahgholi, N. Al-Qudami, J. Andreasson, S. Aplin, S. Awel, K. Ayyer, S. Bajt, I. Barák, S. Bari, J. Bielecki, S. Botha, D. Boukhelef, W. Brehm, S. Brockhauser, I. Cheviakov, M. A. Coleman, F. Cruz-Mazo, C. Danilevski, C. Darmanin, R. B. Doak, M. Domaracky, K. Dörner, Y. Du, H. Fangohr, H. Fleckenstein, M. Frank, P. Fromme, A. M. Gañán-Calvo, Y. Gevorkov, K. Giewekemeyer, H. M. Ginn, H. Graafsma, R. Graceffa, D. Greiffenberg, L. Gumprecht, P. Göttlicher, J. Hajdu, S. Hauf, M. Heymann, S. Holmes, D. A. Horke, M. S. Hunter, S. Imlau, A. Kaukher, Y. Kim, A. Klyuev, J. Knoška, B. Kobe, M. Kuhn, C. Kupitz, J. Küpper, J. M. Lahey-Rudolph, T. Laurus, K. Le Cong, R. Letrun, P. L. Xavier, L. Maia, F. R. N. C. Maia, V. Mariani, M. Messerschmidt, M. Metz, D. Mezza, T. Michelat, G. Mills, D. C. F. Monteiro, A. Morgan, K. Mühlig, A. Munke, A. Münnich, J. Nette, K. A. Nugent, T. Nuguid, A. M. Orville, S. Pandey, G. Pena, P. Villanueva-Perez, J. Poehlsen, G. Previtali, L. Redecke, W. M. Riekehr, H. Rohde, A. Round, T. Safenreiter, I. Sarrou, T. Sato, M. Schmidt, B. Schmitt, R. Schönherr, J. Schulz, J. A. Sellberg, M. M. Seibert, C. Seuring, M. L. Shelby, R. L. Shoeman, M. Sikorski, A. Silenzi, C. A. Stan, X. Shi, S. Stern, J. Sztuk-Dambietz, J. Szuba, A. Tolstikova, M. Trebbin, U. Trunk, P. Vagovic, T. Ve, B. Weinhausen, T. A. White, K. Wrona, C. Xu, O. Yefanov, N. Zatsepin, J. Zhang, M. Perbandt, A. P. Mancuso, C. Betzel, H. Chapman, and A. Barty, "Megahertz serial crystallography," Nat. Commun. **9**(1), 4025 (2018).
10. M. Schmidt, "Mix and Inject: Reaction Initiation by Diffusion for Time-Resolved Macromolecular Crystallography," Adv. Condens. Matter Phys. **2013**, 167276 (2013).
11. K. Pande, C. D. M. Hutchison, G. Groenhof, A. Aquila, J. S. Robinson, J. Tenboer, S. Basu, S. Boutet, D. P. DePonte, M. Liang, T. A. White, N. A. Zatsepin, O. Yefanov, D. Morozov, D. Oberthuer, C. Gati, G. Subramanian, D. James, Y. Zhao, J. Koralek, J. Brayshaw, C. Kupitz, C. Conrad, S. Roy-Chowdhury, J. D. Coe, M. Metz, P. L. Xavier, T. D. Grant, J. E. Koglin, G. Ketawala, R. Fromme, V. Srajer, R. Henning, J. C. Spence, A. Ourmazd, P. Schwander, U. Weierstall, M. Frank, P. Fromme, A. Barty, H. N. Chapman, K. Moffat, J. J. Van Thor, and M. Schmidt, "Femtosecond structural dynamics drives the trans/cis isomerization in photoactive yellow protein," Science **352**(6286), 725–729 (2016).
12. R. Akre, D. Dowell, P. Emma, J. Frisch, S. Gilevich, G. Hays, P. Hering, R. Iverson, C. Limborg-Deprey, H. Loos, A. Miahnahri, J. Schmerge, J. Turner, J. Welch, W. White, and J. Wu, "Commissioning the Linac Coherent Light Source injector," Phys. Rev. ST Accel. Beams **11**(3), 030703 (2008).
13. D. Pile, "X-rays: First light from SACLA," Nat. Photonics **5**(8), 456–457 (2011).
14. M. Altarelli and A. P. Mancuso, "Structural biology at the European X-ray free-electron laser facility," Philos. Trans. R. Soc. B Biol. Sci. **369**(1647), 20130311 (2014).
15. J. Knoška, L. Adriano, S. Awel, K. R. Beyerlein, O. Yefanov, D. Oberthuer, G. E. Peña Murillo, N. Roth, I. Sarrou, P. Villanueva-Perez, M. O. Wiedorn, F. Wilde, S. Bajt, H. N. Chapman, and M. Heymann, "Ultracompact 3D microfluidics for time-resolved structural biology," Nat. Commun. **11**(1), 657 (2020).
16. F. Mafuné, K. Miyajima, K. Tono, Y. Takeda, J. Y. Kohno, N. Miyauchi, J. Kobayashi, Y. Joti, E. Nango, S. Iwata, and M. Yabashi, "Microcrystal delivery by pulsed liquid droplet for serial femtosecond crystallography," Acta Crystallogr D Struct Biol **72**(4), 520–523 (2016).
17. C. G. Roessler, R. Agarwal, M. Allaire, R. Alonso-Mori, B. Andi, J. F. R. Bachega, M. Bommer, A. S. Brewster, M. C. Browne, R. Chatterjee, E. Cho, A. E. Cohen, M. Cowan, S. Datwani, V. L. Davidson, J. Defever, B. Eaton, R. Ellson, Y. Feng, L. P. Ghislain, J. M. Glownia, G. Han, J. Hattne, J. Hellmich, A. Héroux, M. Ibrahim, J. Kern, A. Kuczewski, H. T. Lemke, P. Liu, L. Majlof, W. M. McClintock, S. Myers, S. Nelsen, J. Olechno, A. M. Orville, N. K. Sauter, A. S. Soares, S. M. Soltis, H. Song, R. G. Stearns, R. Tran, Y. Tsai, M. Uervirojnangkoorn, C. M. Wilmot, V. Yachandra, J. Yano, E. T. Yukl, D. Zhu, and A. Zouni, "Acoustic Injectors for Drop-On-Demand Serial Femtosecond Crystallography," Structure **24**(4), 631–640 (2016).
18. A. Echelmeier, J. Cruz Villarreal, M. Messerschmidt, D. Kim, J. D. Coe, D. Thifault, S. Botha, A. Egatz-Gomez, S. Gandhi, G. Brehm, C. E. Conrad, D. T. Hansen, C. Madsen, S. Bajt, J. D. Meza-Aguilar, D. Oberthür, M. O. Wiedorn, H. Fleckenstein, D. Mendez, J. Knoška, J. M. Martin-Garcia, H. Hu, S. Lisova, A. Allahgholi, Y. Gevorkov, K. Ayyer, S. Aplin, H. M. Ginn, H. Graafsma, A. J. Morgan, D. Greiffenberg, A. Klujev, T. Laurus, J. Poehlsen, U. Trunk, D. Mezza, B. Schmidt, M. Kuhn, R. Fromme, J. Sztuk-Dambietz, N. Raab, S. Hauf, A. Silenzi, T. Michelat, C. Xu, C. Danilevski, A. Parenti, L. Mekinda, B. Weinhausen, G. Mills, P. Vagovic, Y. Kim, H. Kirkwood, R. Bean, J. Bielecki, S. Stern, K. Giewekemeyer, A. R. Round, J. Schulz, K. Dörner, T. D. Grant, V. Mariani, A. Barty, A. P. Mancuso, U. Weierstall, J. C. H. Spence, H. N. Chapman, N. Zatsepin, P. Fromme, R. A. Kirian, and A. Ros, "Segmented flow generator for serial crystallography at the European X-ray free electron laser," Nat. Commun. **11**(1), 4511 (2020).
19. F. D. Fuller, S. Gul, R. Chatterjee, E. Sethe Burgie, I. D. Young, H. Lebrette, V. Srinivas, A. S. Brewster, T. Michels-Clark, J. A. Clinger, B. Andi, M. Ibrahim, E. Pastor, C. De Lichtenberg, R. Hussein, C. J. Pollock, M. Zhang, C. A. Stan, T. Kroll, T. Fransson, C. Weninger, M. Kubin, P. Aller, L. Lassalle, P. Bräuer, M. D. Miller, M. Amin, S. Koroidov, C. G. Roessler, M. Allaire, R. G. Sierra, P. T. Docker, J. M. Glownia, S. Nelson, J. E. Koglin, D. Zhu, M. Chollet, S. Song, H. Lemke, M. Liang, D. Sokaras, R. Alonso-Mori, A. Zouni, J. Messinger, U. Bergmann, A. K. Boal, J. Martin Bollinger, C. Krebs, M. Högbom, G. N. Phillips, R. D. Vierstra, N. K. Sauter, A. M. Orville, J.

Optics EXPRESS

Kern, V. K. Yachandra, and J. Yano, "Drop-on-demand sample delivery for studying biocatalysts in action at X-ray free-electron lasers," Nat. Methods **14**(4), 443–449 (2017).
20. A. Ashkin, "Acceleration and Trapping of Particles by Radiation Pressure," Phys. Rev. Lett. **24**(4), 156–159 (1970).
21. J. Guck, R. Ananthakrishnan, H. Mahmood, T. J. Moon, C. C. Cunningham, and J. Käs, "The optical stretcher: A novel laser tool to micromanipulate cells," Biophys. J. **81**(2), 767–784 (2001).
22. S. A. Tatarkova, A. E. Carruthers, and K. Dholakia, "One-Dimensional Optically Bound Arrays of Microscopic Particles," Phys. Rev. Lett. **89**(28), 283901 (2002).
23. B. J. Black and S. K. Mohanty, "Fiber-optic spanner," Opt. Lett. **37**(24), 5030–5032 (2012).
24. A. Constable, J. Kim, J. Mervis, F. Zarinetchi, and M. Prentiss, "Demonstration of a-fiber-optical light-force trap," Opt. Lett. **18**(21), 1867–1869 (1993).
25. B. Lincoln, S. Schinkinger, K. Travis, F. Wottawah, S. Ebert, F. Sauer, and J. Guck, "Reconfigurable microfluidic integration of a dual-beam laser trap with biomedical applications," Biomed. Microdevices **9**(5), 703–710 (2007).
26. J.-D. Nicolas, J. Hagemann, M. Sprung, and T. Salditt, "The optical stretcher as a tool for single-particle X-ray imaging and diffraction," J. Synchrotron Radiat. **25**(4), 1196–1205 (2018).
27. N. Bellini, K. C. Vishnubhatla, F. Bragheri, L. Ferrara, P. Minzioni, R. Ramponi, I. Cristiani, and R. Osellame, "Femtosecond laser fabricated monolithic chip for optical trapping and stretching of single cells," Opt. Express **18**(5), 4679 (2010).
28. M. Asadi, "Tables," in *Beet-Sugar Handbook* (John Wiley & Sons, Ltd, 2006), pp. 779–801.
29. J. F. Swindells, C. F. Snyder, R. C. Hardy, and P. E. Golden, "Viscosities of Sucrose Solutions at Various Temperatures: Tables of Recalculated Values," United States National Bureau of Standards (1958).
30. D. B. Allan, T. Caswell, N. C. Keim, and C. M. van der Wel, "soft-matter/trackpy: Trackpy v0.4.2," https://doi.org/10.5281/zenodo.3492186 (2019).
31. J. C. Crocker and D. G. Grier, "Methods of Digital Video Microscopy for Colloidal Studies," J. Colloid Interface Sci. **179**(1), 298–310 (1996).
32. M. D. M. Mahdavimanesh, A.R. Noghrehabadi, M. Behbahaninejad, and G. Ahmadi, "Lagrangian Particle Tracking: Model Development," Life Sci. J. **10**, 34–41 (2013).
33. D. Hryb, M. Cardozo, S. Ferro, and M. Goldschmit, "Particle transport in turbulent flow using both Lagrangian and Eulerian formulations," Int. Commun. Heat Mass Transf. **36**(5), 451–457 (2009).
34. C. Multiphysics, "Introduction to comsol multiphysics®," COMSOL Multiphysics, Burlington, MA, accessed Feb 9, 2018 (1998).
35. C. E. Willert and M. Gharib, "Digital particle image velocimetry," Exp. Fluids **10**(4), 181–193 (1991).
36. T. A. Nieminen, V. L. Y. Loke, A. B. Stilgoe, G. Knöner, A. M. Brańczyk, N. R. Heckenberg, and H. Rubinsztein-Dunlop, "Optical tweezers computational toolbox," J. Opt. A: Pure Appl. Opt. **9**(8), S196–S203 (2007).
37. H. G. Tompkins, S. Smith, and D. Convey, "Optimizing the ellipsometric analysis of a transparent layer on glass," Surf. Interface Anal. **29**(12), 845–850 (2000).
38. S. Awel, S. Lavin-Varela, N. Roth, D. A. Horke, A. V. Rode, R. A. Kirian, J. Küpper, and H. N. Chapman, "Optical funnel to guide and focus virus particles for X-ray laser imaging," arXiv Prepr. arXiv2102.02899 (2021).
39. G. Goddard, J. C. Martin, S. W. Graves, and G. Kaduchak, "Ultrasonic particle-concentration for sheathless focusing of particles for analysis in a flow cytometer," Cytometry **69A**(2), 66–74 (2006).
40. R. Scott, P. Sethu, and C. K. Harnett, "Three-dimensional hydrodynamic focusing in a microfluidic Coulter counter," Rev. Sci. Instrum. **79**(4), 046104 (2008).
41. J. Rossbach, "Observation of self-amplified spontaneous emission in the wavelength range from 80 to 180 nm at the TESLA test facility FEL at DESY," Nucl. Instruments Methods Phys. Res. Sect. A Accel. Spectrometers, Detect. Assoc. Equip. **475**(1-3), 13–19 (2001).